Optical bistability in a silicon nitride microring integrated with 2D $PtSe_2$

Jiaqi Wang (王佳琦)[1,*], Yingqi Xu (徐滢淇)[1], Zhijian Mao (毛志坚)[1], Guoxian Wu (吴国贤)[1], Rongxiang Guo (郭荣翔)[2,3], Xu Li (李旭)[1], Yu Du (杜宇)[1], Youfu Geng (耿优福)[1], Xuejin Li (李学金)[1], Hon Ki Tsang (曾汉奇)[4], and Zhenzhou Cheng (程振洲)[2,3,5,6]**

[1] College of Physics and Optoelectronic Engineering, Shenzhen University, Shenzhen 518060, China
[2] School of Precision Instrument and Optoelectronics Engineering, Tianjin University, Tianjin 300072, China
[3] Key Laboratory of Optoelectronics Information Technology, Ministry of Education, Tianjin 300072, China
[4] Department of Electronic Engineering, The Chinese University of Hong Kong, Shatin, Hong Kong
[5] Georgia Tech-Shenzhen Institute, Tianjin University, Shenzhen 518055, China
[6] School of Physics and Electronic Engineering, Xinjiang Normal University, Urumqi, Xinjiang 830054, China
[*] Corresponding author: jqwang@szu.edu.cn; ** corresponding author: zhenzhoucheng@tju.edu.cn
Received Month X, XXXX; accepted Month X, XXXX; posted online Month X, XXXX

Optical bistability can be used to explore key components of all-optical information processing systems, such as optical switches and optical random memories. The hybrid integration of emerged two-dimensional layered $PtSe_2$ with waveguides is promising for the applications. We demonstrated the optical bistability in the $PtSe_2$-on-silicon nitride microring resonator induced by a thermo-optic effect. The fabricated device has a resonance-increasing rate of 6.8 pm/mW with increasing optical power. We also established a theoretical model to explain the observation and analyze the device's performance. The study is expected to provide a new scheme for realizing all-optical logic devices in next-generation information processing systems.
Keywords: Optical bistability; waveguide-integrated $PtSe_2$ device; nonlinear optics
DOI: 10.3788/COLXXXXXX.XXXXXX.

1. Introduction

The integration of two-dimensional (2D) materials, such as graphene and transition metal dichalcogenides (TMDCs), with photonic integrated circuits has been emerging for applications in optical modulation [1], detection [2,3], and nonlinear signal processing [4,5], owing to the unique optical and electronic properties [6,7] of 2D materials, the giant interaction between 2D materials and light in waveguide devices [8,9], as well as, the CMOS-compatible device fabrication processes. $PtSe_2$ is a newly discovered group-ten TMDC with a tunable bandgap, carrier mobility of more than 16300 $cm^2V^{-1}s^{-1}$ [10], and stable physical and chemical properties[11,12], which makes $PtSe_2$ promising for various optoelectronic applications [7,12]. To date, waveguide-integrated $PtSe_2$ devices have been explored for optoelectronic applications of light modulation [13] and photodetection [14,15].

On the other hand, optical bistability can be used to construct all-optical switches, optical memories, and all-optical logic gates, which are believed to break through the bottleneck of information exchange in future communication and computing systems, playing a crucial role as the core of the next-generation communication and signal processing systems [16]. Optical bistability was realized in silicon waveguide devices at the beginning of this century [17]. To further enhance the on-chip optical bistability, graphene-on-waveguide structures have been applied for developing bistable devices. For example, by integrating graphene on the waveguide-integrated Fabry–Perot resonator [18] and microring resonator (MRR) [19], the photo-induced Joule heating in graphene can lead to enhanced effective thermal nonlinear index compared with the bare silicon waveguides. Besides, optical bistability with low input power requirement induced by the Kerr effect in graphene has been theoretically studied in the graphene-on-silicon slot microring resonator [20]. However, the optical bistability has seldom been reported based on waveguide-integrated $PtSe_2$ devices.

In this paper, we studied an integrated nonlinear optical device based on 2D few-layer $PtSe_2$-on-silicon nitride MRR. We measured the transmission spectra of the silicon nitride MRRs before and after covering the $PtSe_2$ film and calculated the absorption coefficients of the fabricated devices. We selected a representative device to measure its transmission curve while gradually increasing the optical power. The resonance shifts to longer wavelengths linearly with the input power, and a clear optical bistability effect was observed. Besides, we used the time-domain coupled mode theory (CMT) to simulate the thermo-optic effect in the device, which agrees well with the experimental results. The subsequent finite element method (FEM) simulation also shows that the integration of $PtSe_2$ greatly enhances the photo-thermal conversion in the waveguide device. The study is expected to provide a useful reference for developing subsequent nonlinear devices for all-optical signal processing applications.

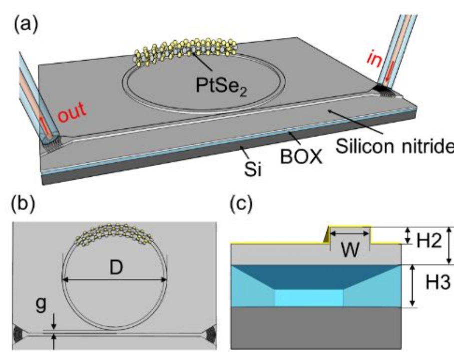

FIG. 1. Schematic of the $PtSe_2$-on-silicon nitride MRR. (a) Three-dimensional view of the device. (b) Top view of the device. (c) Cross-section view of the waveguide.

2. Results and discussion

We designed and fabricated the $PtSe_2$-on-silicon nitride MRR based on the standard nanofabrication technology and home-developed wet transfer method. We first fabricated silicon nitride MRRs by using electron beam lithography and ICP-DRIE. The low-pressure chemical vapor deposited (CVD) top silicon nitride layer is 720 nm thick (H1), the buried oxide (BOX) is 4 μm thick (H3), and the etching depth of the silicon nitride layer is 400 nm (H2), as shown in Fig. 1. The gap between the bus waveguide and the microring is 390 nm (g). The width of the waveguide (W) and the diameter (D) of the MRR are 1.2 μm and 200 μm. A pair of focusing one-dimensional grating couplers is used for the fiber-to-waveguide optical coupling. Next, we covered the MRR with commercial CVD-grown five-layer $PtSe_2$ film on the sapphire substrate (Six Carbon Technology Shenzhen). To transfer the material, a layer of polymethyl methacrylate (PMMA) was spin-coated on the surface of the $PtSe_2$ sample, and the PMMA layer was heated and cured to form a solid protection layer. Then the sample was immersed in the KOH solution to separate the PMMA-on-$PtSe_2$ layer from the sapphire substrate. After cleaning in the deionized water, the PMMA-on-$PtSe_2$ layer was transferred onto the silicon nitride chip. Then the chip was drying in the air. Finally, the PMMA was removed with an acetone solution. The flowchart for the fabrication process is shown in Fig. S1 in Supplementary Material.

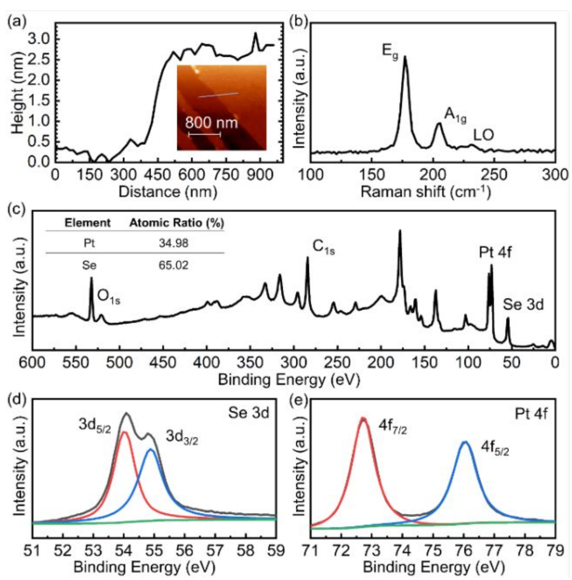

FIG. 2. Characterization of the five-layer $PtSe_2$ on the surface of the silicon nitride chip. (a) The AFM characterization of the $PtSe_2$ film. (b) The Raman spectrum of the $PtSe_2$ film measured by using a Raman spectrometer with a pump wavelength of 785 nm. (c) The measurement result of the XPS full spectrum. (d) and (e) are the Gaussian fitting curves of the Pt 4f peak and the Se 3d peak in (c).

Next, we characterized the five-layer $PtSe_2$ film on the surface of the silicon nitride chip. The thickness of the $PtSe_2$ film was measured to be ~2.5 nm by using atomic force microscopy (AFM), as shown in Fig. 2(a). Fig. 2(b) shows the Raman spectrum of the $PtSe_2$ film on the surface of the silicon nitride chip. Three major Raman peaks appeared at $177cm^{-1}$, $206cm^{-1}$, and $225cm^{-1}$, related to the E_g, A_{1g}, and LO vibration modes of Se atoms respectively, and the locations of Raman peaks were consistent with the previous report [21]. X-ray photoelectron spectroscopy (XPS) analysis was also performed to characterize the $PtSe_2$ film further. As shown in Fig. 2(c), C, O, Pt, and Se peaks mainly existed in the film. The peaks of C_{1s} and O_{1s} come from the air absorbed by the surface of the $PtSe_2$ film. Two peaks of 72.72eV and 76.02eV corresponding to Pt $4f_{7/2}$ and Pt $4f_{5/2}$ were obtained by Gaussian fitting of the Pt 4f peak, as shown in Fig. 2(d). The fitting of the Se 3d peak in Fig. 2(e) also results in two main peaks located at 54.02eV and 54.88eV, corresponding to Se $3d_{5/2}$ and Se $3d_{3/2}$. The atomic numbers of Pt and Se were calculated based on the measured spectra, as shown in the inset table of Fig. 2(c), which was consistent with the theoretical values [21].

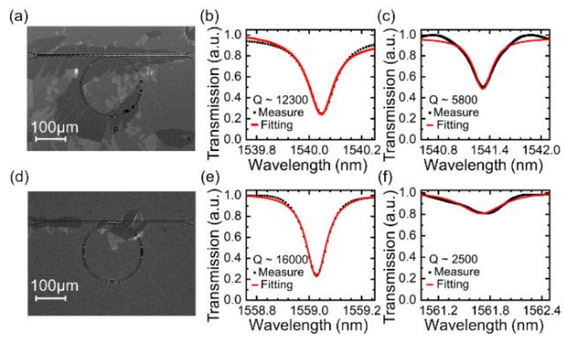

FIG. 3. Characterization of the $PtSe_2$-on-silicon nitride MRRs. (a) and (d) are the SEM images of two MRRs with the $PtSe_2$ film coverage, with estimated lengths of the material covered of 125 μm and 471 μm. (b) and (c) are the transmission spectra of the MRR in (a) before and after the $PtSe_2$ film transfer. (e) and (f) are the transmission spectra of the MRR in (d) before and after the $PtSe_2$ film transfer.

Next, we characterized the optical absorption of the $PtSe_2$-on-silicon nitride MRRs. The scanning electron microscopy (SEM) images of the devices are shown in Fig. 3(a) and (d). The wet transfer process resulted in $PtSe_2$ film breakages on the MRRs. The material-covered lengths on the MRRs were estimated as 125 μm (Fig. 3(a)) and 471 μm (Fig. 3(d)) from the contrast of the images. For the MRR in Fig. 3(a), from the Lorentz fittings of the fullwidth at half maximum (FWHM) of the measured resonance (λ_{res}) spectra in Fig. 3(b) and (c), the Q factor is obtained as $Q = \lambda_{res}/$ FWHM, with 12300 and 5800 before and after the $PtSe_2$ film coverage. The transmission spectra of the MRR in Fig. 3(d) before and after the $PtSe_2$ film integration are shown in Fig. 3(e) and (f). The quality (Q) factor decreases from 16000 to 2500 after the $PtSe_2$ film integration. Combined with the estimated $PtSe_2$ film covered length, and the measured transmission spectra before and after the $PtSe_2$ film integration, the optical absorption coefficients of the $PtSe_2$-on-silicon nitride waveguide were calculated [22] as 172dB/cm (Fig. 3(a)) and 171dB/cm (Fig. 3(d)). The resonances have redshifts after the $PtSe_2$ film integration due to the effective refractive index change induced by the $PtSe_2$ film. We also simulated the optical absorption coefficient of the $PtSe_2$-on-silicon nitride waveguide to be ~179 dB/cm, by using the FEM simulator (COMSOL Multiphysics) with the complex dielectric constant of the 5-layer $PtSe_2$ in the previous study [21], which was measured by using the spectroscopic ellipsometry method. The simulation result agrees well with the experimental estimation.

To measure the nonlinear property of the fabricated device, we set up an experimental system as shown in Fig. 4(a). We used a variable optical attenuator (VOA) to vary the input optical power, and the 1% output of the 1:99 optical coupler to monitor the input power with a power meter (PM1). The coupling efficiency of the grating coupler at 1550 nm wavelengths is ~-5.5 dB. The input power in the following experiment refers to the optical power coupled into the bus waveguide from the grating coupler. We chose the device shown in Fig. 3(a) for the optical-bistability exploration. We started by setting the output power of the erbium-doped fiber amplifier (EDFA) to a high value that the device can withstand, while the VOA attenuation was set to the maximum attenuation. In this way, we can start the measurement at a low input power, ensuring a stable and continuous tuning of the input power. The measured transmission spectra for different input powers are shown in Fig. 4(b). As the input power increases, the resonance shifts to longer wavelengths, with a linearly fitted slope of ~6.8 pm/mW, as shown in Fig. 4(c). Besides, as the optical power increases, the resonance curve is no longer symmetrical, and eventually, there is a significant power jump on the longer wavelength side, which indicates the emergence of the bistable state.

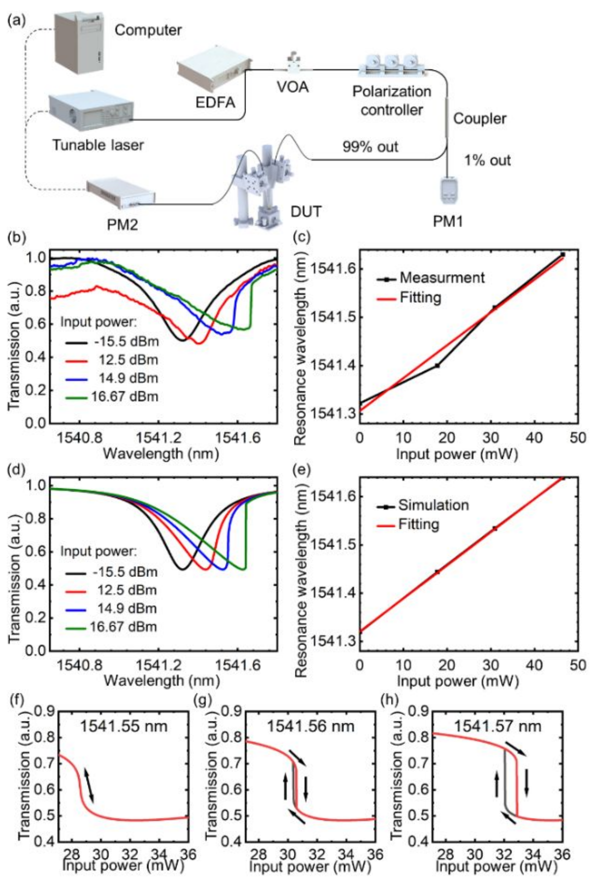

FIG. 4. Optical nonlinearity measurement and simulation results. (a) Schematic of the experimental setup. (b) Measured transmission spectra under different input power levels. (c) The resonant wavelength at different input powers. (d) Simulated transmission spectra under different input powers using the time-domain CMT method. (e) Simulated resonant wavelengths at different input powers. (f)-(h) Hysteresis loop simulations for the input wavelengths of 1541.55 nm, 1541.56 nm, and 1541.57 nm. Arrows in (f)-(h) indicate the directions of the input power variations.

To further evaluate the nonlinear effect in the $PtSe_2$-on-silicon nitride MRR, we used the time-domain CMT [23,24] method to calculate the energy distribution ($|a|^2$) in the microring cavity with the input power in the bus waveguide (P_{in}), and the transmission spectrum of the MRR (T_{trans}). We established the CMT model as follows [25,26],

$$\frac{1}{Q_0} = \frac{1}{Q_{inst}} + \frac{1}{Q_{ext}} \tag{1}$$

$$\frac{2}{\tau_{ext(inst)}} = \frac{\omega_0'}{Q_{ext(inst)}} \tag{2}$$

$$\omega_0' = \frac{2\pi c}{\lambda_0 + \Delta\lambda_{therm} + \Delta\lambda_{Kerr}} \tag{3}$$

$$\Delta\lambda_{therm} = \frac{2|a|^2 \tau_{linear}^{-1} \lambda_0 R}{n_0} \frac{\partial n}{\partial T} \tag{4}$$

$$\Delta\lambda_{Kerr} = \frac{|a|^2 n_2 \lambda_0 c}{n_0 n_g V} \tag{5}$$

$$|a|^2 = \frac{2\tau_{ext}^{-1} P_{in}}{(\omega - \omega_0')^2 + \left(\tau_{ext}^{-1} + \tau_{inst}^{-1} + \tau_{linear}^{-1}\right)^2} \tag{6}$$

$$T_{\mathrm{trans}} = \frac{(\omega - \omega_0')^2 + (\tau_{ext}^{-1} + \tau_{linear}^{-1} - \tau_{inst}^{-1})^2}{(\omega - \omega_0')^2 + \left(\tau_{ext}^{-1} + \tau_{inst}^{-1} + \tau_{linear}^{-1}\right)^2} \tag{7}$$

where Q_0 is the loaded Q factor of the MRR, τ_{ext} and Q_{ext} are related to the intra-cavity mode reduction rate caused by the light coupling output, τ_{inst} and Q_{inst} are related to the dissipation rate caused by the intrinsic loss in the microring cavity, τ_{inst} can be regarded as the time that the mode amplitude attenuates to $1/e$ of the initial amplitude under the effect of the intrinsic loss in the microring cavity. ω_0' is the resonant frequency, considering the thermo-optic effect ($\Delta\lambda_{therm}$) and Kerr effect ($\Delta\lambda_{Kerr}$). λ_0 is the resonance without nonlinear effect (i.e., at low input powers), τ_{linear} is the amplitude loss rate caused by the linear optical loss, R is the thermal resistance of the MRR, n_0 is the refractive index of the waveguide, $\partial n/\partial T$ is the thermo-optic coefficient, n_2 is the Kerr coefficient of silicon nitride, c is the speed of vacuum light, ω is the angular frequency of the input light. n_g and V are the group index and the mode volume in the MRR cavity, which are calculated by the frequency-difference time-domain (FDTD) method (Lumerical FDTD). The values of the parameters are shown in Table 1. Specifically, parameters of Q_{ext}, Q_{inst}, τ_{linear}, and R were obtained by fitting the measurement of the transmission spectrum of the $PtSe_2$-on-silicon nitride MRR at the low input power of -15.5 dBm. The simulation results are shown in Fig. 4(d). The transmission spectrum becomes unsymmetrical at high input powers, with a resonance increasing slope of 6.85 pm/mW (shown in the linear fit in Fig. 4(e)), which is consistent with the measurement result, indicating that our model can well describe the nonlinear effects in the device. Besides, it can be known from Eqs. (4)

and (5) that the resonance shift due to the thermo-optic effect dominates, while the Kerr effect is almost negligible. We also calculated the power transmission of the device for different input wavelengths based on the time-domain CMT model. As shown in Fig. 4(f), with an input wavelength of 1541.55 nm, there is always only one solution to the equations with the change of the input power, which means that the MRR has only one steady state, which is the same to the shorter wavelengths. At the longer input wavelength of 1541.56 nm, a hysteresis loop appears and represents the appearance of bistability (Fig. 4(g)). With further increasing the input wavelength to 1541.57 nm, the hysteresis loop is extended and the gap between the two steady states increases (Fig. 4(h)). Besides, the stronger thermal-optic effect can lead to the redshift of the bistable threshold wavelength and decrease of the bistable threshold power while the reduction in width and area of the hysteresis loop. The device itself works like an optical static random-access memory. Decreasing or increasing the input optical power can be regarded as writing data, after which the device can hold the written data by setting the input power between the two edges of the hysteresis loop, and the data can be read by detecting the output of the device. We also measured the switching time of the bistable state to be ~30 μs by synchronously recording the input and output powers with the two power-sensor ports of the optical power meter (N7744A) while tuning the input power.

Table 1. Parameters and sources used in CMT simulation.

Parameter	Value	Source
Q_0	5800	[Measurement]
Q_{ext}	40324	[Measurement, CMT [27,28]]
Q_{inst}	6774	[Measurement, CMT [27,28]]
τ_{linear} (s)	1.6×10^{-9}	[Measurement, CMT [27,28]]
R (K/mW)	105	[Measurement, CMT [27,28]]
n_0	1.9965	[Reference [29]]
n_2 (m^2/W)	2.6×10^{-19}	[Reference [30]]
n_g	2.05	[FDTD simulation]
V (m^3)	8.4754×10^{-16}	[FDTD simulation]
$\partial n/\partial T$ (1/K)	2.51×10^{-5}	[Reference [31]]

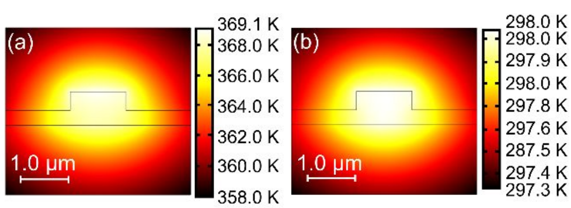

FIG. 5. Electromagnetic thermal simulation results of the waveguide cross-section. (a) and (b) are temperature distributions of the $PtSe_2$-on-silicon nitride waveguide cross-section and the bare waveguide cross-section.

Finally, we performed a simulation of the photothermal effect in the waveguide using the FEM simulator (COMSOL Multiphysics) with the electromagnetic heating module. We modeled the waveguide cross-section and simulated the cases with and without the $PtSe_2$ film integration. In the simulation, the electromagnetic loss was used as the heat source for heat transfer calculations and then the temperature distribution can be obtained. We gave the model an initial input light source of about 30 mW and set the ambient temperature to 293.15 K. The thermal conductivity of air, silicon nitride, $PtSe_2$, and BOX were chosen as 0.026 m·K, 29 m·K, 51 m·K [32], and 1.4 m·K. The conductivity of $PtSe_2$ film was set to 1×10^{-5} S/m [33]. The simulation results are shown in Fig. 5. The average temperature of the waveguide region is about 366.2 K, which is a significant improvement compared with the case of bare silicon nitride waveguide with an average temperature of 297.9 K. This result also indicates that the application of $PtSe_2$ film can enhance the photothermal conversion in the waveguide. The results demonstrate the application and potential of $PtSe_2$-based bistable devices in all-optical signal processing.

3. Conclusion

In summary, we have studied the optical bistability in the five-layer $PtSe_2$-on-silicon nitride MRR. The absorption coefficient of the $PtSe_2$-on-silicon nitride waveguide was obtained from the transmission spectra of the MRR with/without $PtSe_2$ film coverage at the low input optical power. With increasing the input power, the resonance of the $PtSe_2$-on-silicon nitride MRR has redshifts, and the transmission spectrum becomes unsymmetrical, showing the optical bistability. We have also theoretically studied the nonlinear effects in the device through developing the time-domain CMT model, the results were consistent with the measurement results. Besides, the FEM simulation also shows that the addition of the five-layer $PtSe_2$ film significantly enhances the photothermal conversion in the waveguide device. The results obtained in this study provide some references to the combination of $PtSe_2$ with waveguide devices and its mechanism of action, which will help us to advance the application of TMDCs thin film materials in integrated photonics, as well as provide a new direction of exploration for integrated optoelectronic devices.

Reference

1. Y. Ding, X. Guan, X. Zhu, H. Hu, S. I. Bozhevolnyi, L. K. Oxenlowe, K. J. Jin, N. A. Mortensen, and S. Xiao, "Efficient electro-optic modulation in low-loss graphene-plasmonic slot waveguides," Nanoscale **9,** 15576 (2017).
2. N. Flory, P. Ma, Y. Salamin, A. Emboras, T. Taniguchi, K. Watanabe, J. Leuthold, and L. Novotny, "Waveguide-integrated van der Waals heterostructure photodetector at telecom wavelengths with high speed and high responsivity," Nat. Nanotechnol. **15,** 118 (2020).
3. J. Wang, Z. Cheng, Z. Chen, X. Wan, B. Zhu, H. K. Tsang, C. Shu, and J. Xu, "High-responsivity graphene-on-silicon slot waveguide photodetectors," Nanoscale **8,** 13206 (2016).
4. J. Wu, Y. Yang, Y. Qu, L. Jia, Y. Zhang, X. Xu, S. T. Chu, B. E. Little, R. Morandotti, B. Jia, and D. J. Moss, "2D Layered Graphene Oxide Films Integrated with Micro-Ring Resonators for Enhanced Nonlinear Optics," Small **16,** e1906563 (2020).
5. Q. Feng, H. Cong, B. Zhang, W. Wei, Y. Liang, S. Fang, T. Wang, and J. Zhang, "Enhanced optical Kerr nonlinearity of graphene/Si hybrid waveguide," Appl. Phys. Lett **114,** 071104 (2019).
6. M. M. Ugeda, A. J. Bradley, S. F. Shi, F. H. da Jornada, Y. Zhang, D. Y. Qiu, W. Ruan, S. K. Mo, Z. Hussain, Z. X.

Shen, F. Wang, S. G. Louie, and M. F. Crommie, "Giant bandgap renormalization and excitonic effects in a monolayer transition metal dichalcogenide semiconductor," Nat. Mater. **13,** 1091 (2014).
7. T. Y. Su, H. Medina, Y. Z. Chen, S. W. Wang, S. S. Lee, Y. C. Shih, C. W. Chen, H. C. Kuo, F. C. Chuang, and Y. L. Chueh, "Phase-Engineered $PtSe_2$-Layered Films by a Plasma-Assisted Selenization Process toward All $PtSe_2$-Based Field Effect Transistor to Highly Sensitive, Flexible, and Wide-Spectrum Photoresponse Photodetectors," Small **14,** 1800032 (2018).
8. X. Gan, K. F. Mak, Y. Gao, Y. You, F. Hatami, J. Hone, T. F. Heinz, and D. Englund, "Strong Enhancement of Light-Matter Interaction in Graphene Coupled to a Photonic Crystal Nanocavity," Nano Lett. **12,** 5626 (2012).
9. Z. Shi, L. Gan, T. H. Xiao, H. L. Guo, and Z. Y. Li, "All-Optical Modulation of a Graphene-Cladded Silicon Photonic Crystal Cavity," ACS Photonics **2,** 1513 (2015).
10. Y. Zhao, J. Qiao, Z. Yu, P. Yu, K. Xu, S. P. Lau, W. Zhou, Z. Liu, X. Wang, W. Ji, and Y. Chai, "High-Electron-Mobility and Air-Stable 2D Layered $PtSe_2$ FETs," Adv. Mater. **29,** 1604230 (2017).
11. A. Avsar, A. Ciarrocchi, M. Pizzochero, D. Unuchek, O. V. Yazyev, and A. Kis, "Defect induced, layer-modulated magnetism in ultrathin metallic $PtSe_2$," Nat. Nanotechnol. **14,** 674 (2019).
12. Z. Wang, Z. Dong, Y. Gu, Y. H. Chang, L. Zhang, L. J. Li, W. Zhao, G. Eda, W. Zhang, G. Grinblat, S. A. Maier, J. K. Yang, C. W. Qiu, and A. T. Wee, "Giant photoluminescence enhancement in tungsten-diselenide-gold plasmonic hybrid structures," Nat. Commun. **7,** 11283 (2016).
13. K. Wei, D. Li, Z. Lin, Z. Cheng, Y. Yao, J. Guo, Y. Wang, Y. Zhang, J. Dong, H. Zhang, and X. Zhang, "All-optical PtSe2 silicon photonic modulator with ultra-high stability," Photonics Res. **8,** 1189 (2020).
14. S. Parhizkar, M. Prechtl, A. L. Giesecke, S. Suckow, S. Wahl, S. Lukas, O. Hartwig, N. Negm, A. Quellmalz, K. Gylfason, D. Schall, M. Wuttig, G. S. Duesberg, and M. C. Lemme, "Two-Dimensional Platinum Diselenide Waveguide-Integrated Infrared Photodetectors," ACS Photonics **9,** 859 (2022).
15. Y. Wang, Z. J. Yu, Y. Y. Tong, B. L. Sun, Z. Y. Zhang, J. B. Xu, X. K. Sun, and H. K. Tsang, "High-speed infrared two-dimensional platinum diselenide photodetectors," Appl. Phys. Lett **116,** 211101 (2020).
16. B. Li, M. I. Memon, G. Mezosi, Z. Wang, M. Sorel, and S. Yu, "All-optical Digital Logic Gates using Bistable Semiconductor Ring Lasers," J. Opt. Commun. **30,** 190 (2009).
17. V. R. Almeida and M. Lipson, "Optical bistability on a silicon chip," Opt. Lett. **29,** 2387 (2004).
18. C. Horvath, D. Bachman, R. Indoe, and V. Van, "Photothermal nonlinearity and optical bistability in a graphene-silicon waveguide resonator," Opt. Lett. **38,** 5036 (2013).
19. Y. Gao, W. Zhou, X. Sun, H. K. Tsang, and C. Shu, "Cavity-enhanced thermo-optic bistability and hysteresis in a graphene-on-Si_3N_4 ring resonator," Opt. Lett. **42,** 1950 (2017).
20. T. Christopoulos, O. Tsilipakos, and E. E. Kriezis, "Low-power bistability in graphene-comprising 3D photonic resonant circuits," J. Appl. Phys. **122,** 233101 (2017).
21. J. Xie, D. Zhang, X.-Q. Yan, M. Ren, X. Zhao, F. Liu, R. Sun, X. Li, Z. Li, S. Chen, Z.-B. Liu, and J.-G. Tian, "Optical properties of chemical vapor deposition-grown $PtSe_2$ characterized by spectroscopic ellipsometry," 2D Materials **6,** 035011 (2019).
22. J. Q. Wang, Z. Z. Cheng, C. Shu, and H. K. Tsang, "Optical Absorption in Graphene-on-Silicon Nitride Microring Resonators," IEEE Photonics Technol. Lett. **27,** 1765 (2015).
23. H. A. Haus, *Waves and fields in optoelectronics*, Prentice-Hall series in solid state physical electronics (Prentice-Hall, Englewood Cliffs, NJ, 1984), p. 402.
24. T. Uesugi, B. S. Song, T. Asano, and S. Noda, "Investigation of optical nonlinearities in an ultra-high-Q Si nanocavity in a two-dimensional photonic crystal slab," Opt. Express **14,** 377 (2006).
25. X. Sun, X. Zhang, C. Schuck, and H. X. Tang, "Nonlinear optical effects of ultrahigh-Q silicon photonic nanocavities immersed in superfluid helium," Sci. Rep. **3,** 1436 (2013).
26. C. Manolatou, M. J. Khan, S. Fan, P. R. Villeneuve, H. A. Haus, and J. D. Joannopoulos, "Coupling of modes analysis of resonant channel add-drop filters," IEEE J. Quantum Electron. **35,** 1322 (1999).
27. A. Chutinan, M. Mochizuki, M. Imada, and S. Noda, "Surface-emitting channel drop filters using single defects in two-dimensional photonic crystal slabs," Appl. Phys. Lett **79,** 2690 (2001).
28. T. Gu, M. Yu, D.-L. Kwong, and C. W. Wong, "Molecular-absorption-induced thermal bistability in PECVD silicon nitride microring resonators," Opt. Express **22,** 18412 (2014).
29. K. Luke, Y. Okawachi, M. R. Lamont, A. L. Gaeta, and M. Lipson, "Broadband mid-infrared frequency comb generation in a Si_3N_4 microresonator," Opt. Lett. **40,** 4823 (2015).
30. D. J. Moss, R. Morandotti, A. L. Gaeta, and M. Lipson, "New CMOS-compatible platforms based on silicon nitride and Hydex for nonlinear optics," Nat. Photonics **7,** 597 (2013).
31. K. Johnson, N. Alshamrani, D. Almutairi, A. Grieco, C. Horvath, J. N. Westwood-Bachman, A. McKinlay, and Y. Fainman, "Determination of the nonlinear thermo-optic coefficient of silicon nitride and oxide using an effective index method," Opt. Express **30,** 46134 (2022).
32. S. Yin, W. Zhang, C. Tan, L. Chen, J. Chen, G. Li, H. Zhang, Y. Zhang, W. Wang, and L. Li, "Thermal Conductivity of Few-Layer PtS_2 and $PtSe_2$ Obtained from Optothermal Raman Spectroscopy," J. Phys. Chem. C **125,** 16129 (2021).
33. L. Wang, S. Zhang, N. McEvoy, Y. Sun, J. Huang, Y. Xie, N. Dong, X. Zhang, I. M. Kislyakov, J. M. Nunzi, L. Zhang, and J. Wang, "Nonlinear Optical Signatures of the Transition from Semiconductor to Semimetal in $PtSe_2$," Laser & Photonics Rev. **13,** 1900052 (2019).

Funding Sources. This work was supported by the National Natural Science Foundation of China (62161160335, 62175179), the Natural Science Foundation of Guangdong Province, China (2023A1515011189, 2022B1515130002), Hong Kong Research Grants Council Research Grants (N_CUHK423/21), and Science and Technology Plan Project of Shenzhen (JCYJ20230808105007015).